

NJC

Accepted Manuscript



This is an *Accepted Manuscript*, which has been through the Royal Society of Chemistry peer review process and has been accepted for publication.

Accepted Manuscripts are published online shortly after acceptance, before technical editing, formatting and proof reading. Using this free service, authors can make their results available to the community, in citable form, before we publish the edited article. We will replace this *Accepted Manuscript* with the edited and formatted *Advance Article* as soon as it is available.

You can find more information about *Accepted Manuscripts* in the [Information for Authors](#).

Please note that technical editing may introduce minor changes to the text and/or graphics, which may alter content. The journal's standard [Terms & Conditions](#) and the [Ethical guidelines](#) still apply. In no event shall the Royal Society of Chemistry be held responsible for any errors or omissions in this *Accepted Manuscript* or any consequences arising from the use of any information it contains.



www.rsc.org/njc

Enhanced properties of porous CoFe₂O₄-reduced graphene oxide composite with alginate binder for Li-ion battery applications

Cite this: DOI: 10.1039/x0xx00000x

Received 00th January 2014,
Accepted 00th January 2014

DOI: 10.1039/x0xx00000x

www.rsc.org/

P. Ramesh Kumar^a, Pratap Kollu^{*b}, Chella Santhosh^c, Eswara Varaprasada Rao. K^d,
Do Kyung Kim^{*a} and Andrews Nirmala Grace^{*c}

Porous CoFe₂O₄ nanoclusters with different concentrations of graphene based composites were synthesized by a simple solvothermal process. The electrochemical properties of prepared CoFe₂O₄/reduced graphene oxide (rGO) composites were evaluated by using polyvinylidene fluoride and Na-alginate as binder materials. CoFe₂O₄+20% rGO composite with alginate exhibited high stable capacity of 1040 mAh g⁻¹ at 0.1 C (91 mA g⁻¹) rate with excellent rate capability. The observed enhancement in electrochemical properties of CoFe₂O₄+20% rGO composite with alginate is due to the high stability and good transportation network while charging/discharging.

1. Introduction

Secondary lithium-ion batteries have been rapidly investigated for new generation consumer electronic devices and electric vehicles [1-4]. To achieve high energy and power, metal oxides are used as anode materials for the lithium-ion batteries. Metal oxide conversion anodes are showing enhanced storage capacity compared to conventional carbon anode materials [5-9]. Great efforts have been made to improve the capacity and cyclic performance of ternary metal oxides [MFe₂O₄: M= Ni, Co, Zn & Cu] in the last few years [10-12]. Among all metal oxides spinel cobalt ferrite is a promising anode material for lithium-ion batteries, due to its low cost and high chemical stability. Cobalt ferrites (CoFe₂O₄) possess high theoretical capacity of 914 mAh g⁻¹, but it suffers from a severe drawback of high capacity fading during the cycling. It is known that during the conversion reaction electrode pulverization induced huge volume changes during the charge/discharge processes, leading to poor cycling stability [13-18]. To overcome these problems, researchers have made nanocomposites with carbonaceous material (such as carbon and graphene) and prepare the metal oxides in different morphologies [19-22]. However, it is difficult for the carbon-containing nanocomposites to achieve their full storage capacity [23,24].

In our present work, we used Na-alginate as binder for porous nano-structured CoFe₂O₄/graphene nanocomposite to improve the anode performance of Li-ion battery. Alginate (alginic acid) is a copolymer of 1→4 linked D-mannuronic acid (M) and L-guluronic acid (G) residues. The physical and biological properties of alginate will depend upon their compositions and sequences of M and G monoblocks [25]. The porous CoFe₂O₄

is embedded with different concentrations of graphene by using solvothermal process. The prepared porous CoFe₂O₄/reduced graphene oxide (rGO) nanocomposites were characterized using various techniques such as X-ray diffraction, Fourier transform infrared spectroscopy, Field Emission Scanning Electron Microscope, Transmission Electron Microscope, Thermal gravimetric analysis and Raman spectroscopy. Electrochemical characteristics of the prepared nanocomposites were studied using cyclic voltammetry and galvanostatic charge-discharge measurements. These CoFe₂O₄/rGO (20%) nanocomposite with sodium alginate binders exhibits promising electrochemical performance such as high reversible capacity, excellent cycling performance and good rate capability.

2. Experimental

2.1 Synthesis of CoFe₂O₄/G composites

Initially, graphene oxide (GO) was synthesized from natural flake graphite by a modified Hummers method [26]. In a typical procedure, 2.0 g of graphite powder was kept at 0°C in 100 mL concentrated H₂SO₄ which was containing 4.0 g of sodium nitrate solution in a 500 mL flask. With vigorous stirring, 10.0 g of KMnO₄ was added gradually and the temperature of the mixture was controlled to below 10°C. The reaction mixture was stirred at about 35°C for 2 h until it became pasty brownish, and then diluted with 100 mL of deionized water. The addition of water was performed in an ice bath to keep the temperature below 100°C. Then, the mixture was stirred for 30 min. and 20 mL of 30 wt% H₂O₂ was slowly added to reduce the residual KMnO₄, after which the color of the mixture changed to brilliant yellow. The mixture was

filtered and washed with 800 mL of 5% HCl aqueous solution to remove metal ions followed by 1.0 L of de-ionized water to remove the acid. The resulted solid was dried at 60°C for 24 h. For further purification, the as-obtained GO was re-dispersed in de-ionized water and then was dialyzed for one week to remove residual salts and acids. The schematic representation of total synthesis process is shown in figure 1.

The $\text{CoFe}_2\text{O}_4/\text{rGO}$ nanocomposites with different graphene compositions were synthesized by a solvothermal method using ethylene glycol as solvent. Stoichiometrically calculated amount of GO, $\text{FeCl}_3 \cdot 6\text{H}_2\text{O}$ and $\text{CoCl}_2 \cdot 6\text{H}_2\text{O}$ were dispersed in 150 mL of ethylene glycol (EG) with ultrasonication for 2 h. Subsequently, Na acetate and polyethylene glycol (PEG) were added, followed by stirring for 30 min. The mixture was then transferred to a teflon-lined stainless steel autoclave and heated at 200°C for 10 h. The resultant black product was washed with de-ionized water and ethanol several times by centrifugation and was dried at 45°C in a vacuum oven. All AR-grade precursors were used in the synthesis of $\text{CoFe}_2\text{O}_4/\text{rGO}$ nanocomposites obtained from SD-fine chemicals (99% purity), India.

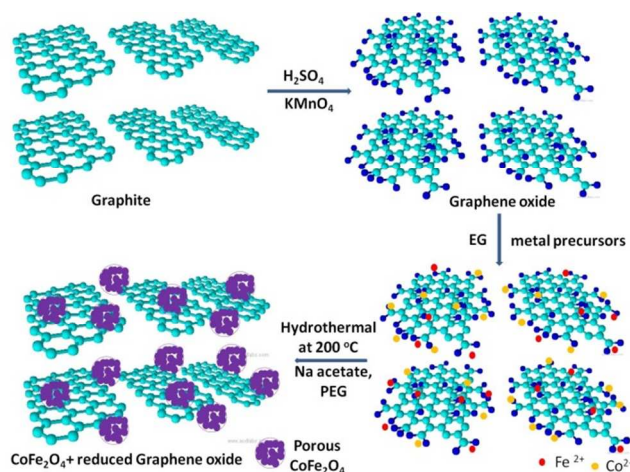


Figure 1: Pictorial representation of synthesis process for $\text{CoFe}_2\text{O}_4/\text{reduced graphene oxide (rGO)}$ composite.

2.2 Characterization

The synthesized porous $\text{CoFe}_2\text{O}_4/\text{rGO}$ composites were characterized using X-ray diffractometer (XRD, X'pert PRO MPD, PANalytical, Philips) with Cu $K\alpha$ radiation ($\lambda=1.54 \text{ \AA}$ at 40 kV and 30 mA). The size and shape of synthesized samples were examined with Field Emission Scanning Electron Microscopy (FESEM)-EDS (JSM-7600F, JEOL). Transmission electron microscope with energy dispersive spectroscopy (TEM), JEOL 2010F HRTEM, Japan, with 200 kV operating voltage was used to capture the morphology and crystallinity of porous $\text{CoFe}_2\text{O}_4/\text{rGO}$ composites sample. Raman measurements were carried out in the back scattered geometry using an (He-Ne laser) laser excitation source emitting at 633 nm with 20 mW power coupled with ARAMIS (Horiba Jobin Yvon, France) micro-Raman spectrometer. The porosity was

determined by using surface area and porosity analyzer (Micromeritics: ASAP 2020).

The electrochemical studies of synthesized porous $\text{CoFe}_2\text{O}_4/\text{rGO}$ composites were analyzed in CR2032 coin cell as half-cell configuration. The composite electrode was prepared by mixing 70 wt% of active material with 20 wt% Super P carbon black (Timcal, super P) and 10 wt% sodium alginate and PVDF binders in a suitable solvent. The obtained slurry was cast on a piece of Cu-foil and cut into circular electrodes. Lithium foil was used as anode and 1 M solution of LiPF₆ in ethylene carbonate and dimethyl carbonate (1:1) was used as electrolyte [LP 30, Merck, Germany]. CR2032 cells were assembled in an argon-filled dry glove box [M. O. Tech., South Korea] using Whatman GF/D borosilicate glass-fiber separator. The cyclic voltammetry and in-situ electrochemical impedance spectroscopy were measured at various potentials during first discharge-charge cycle using Biologic Science Instruments (Model: VMP3, Biologic, France) between 1 MHz to 10 mHz with 5 mV of amplitude. The cells were galvanostatically cycled between 3 V and 0.02 V using BT 2000, Arbin Instrument, USA.

3. Results and discussion

3.1. Structural & microstructural properties

The $\text{CoFe}_2\text{O}_4/\text{rGO}$ composites were successfully prepared by solvothermal process and characterized by the different analysis techniques. Figure 2 shows the XRD patterns for the pure CoFe_2O_4 and composite with different concentrations of rGO and it confirms the phase and purity of CoFe_2O_4 nanoparticles. The peaks are exactly matching with the standard XRD JCPDS data with card number 221086. The observed XRD peaks were indexed to a cubic crystal structure (space group $Fd-3m$). The crystallite size (D) was calculated using the Scherrer Formula: $\beta \cos(\theta) = \lambda k/D$, where β is the full width-at-half-maximum length of the reflection. The calculated crystallite size of the porous pure CoFe_2O_4 sample was found to be 45 nm, which is further confirmed by the SEM micrographs.

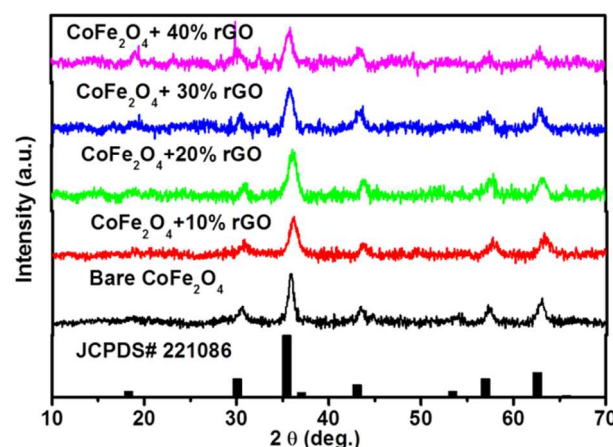


Figure 2: XRD patterns for pure CoFe_2O_4 and composite with different concentrations of rGO

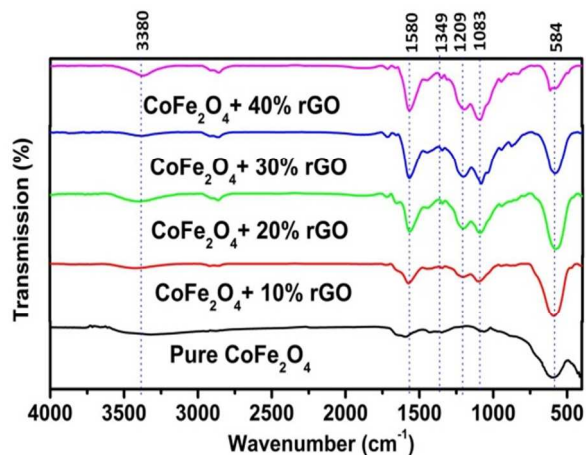


Figure 3: FTIR spectra for pure CoFe_2O_4 and composite with different concentration of rGO.

Fourier transform infrared spectroscopy (FTIR) of the pure CoFe_2O_4 and composite with graphene samples are shown in figure 3. The band at 1580 cm^{-1} is the characteristic peak which can be attributed to the stretching vibration of the unoxidized carbon backbone [27]. The bands at 3380 cm^{-1} and 1349 cm^{-1} are ascribed to the O-H stretching and deformation vibrations respectively. The bands at 1209 cm^{-1} and 1083 cm^{-1} are due to C-O and C-OH stretching vibrations of epoxy groups [28,29]. The absorption peak at around 584 cm^{-1} has also been observed, which are assigned to the M-O band in the cobalt ferrite. The observed FTIR spectrums of pure CoFe_2O_4 and composite with graphene samples were demonstrating the successful reduction of graphene oxide and purity of ternary metal oxides.

Figure 4 shows the FE-SEM images of the pure CoFe_2O_4 and composite with different concentrations of graphene. From figure 4a, the agglomerated porous CoFe_2O_4 nanostructures are found to have a diameter of $\sim 55\text{ nm}$. Figures 4b-e shows the FE-SEM images of the $\text{CoFe}_2\text{O}_4/\text{G}$ composites with 10, 20, 30 and 40% of graphene respectively. EDS spectrum for the pure porous CoFe_2O_4 is shown in figure S1 (see Electronic Supplementary Information†).

HR-TEM images of pure porous CoFe_2O_4 nanostructures at different magnifications are shown in figure 5. The size investigation and selected area electron diffraction (SAED) patterns of the prepared CoFe_2O_4 nanostructures were done using HR-TEM analysis. The HR-TEM images of CoFe_2O_4 nanostructures are shown in Figure 5c, which indicated the formation of agglomerated clusters with $\sim 60\text{ nm}$ in diameter, which is close that observed from FE-SEM. These clusters are made up of few numbers of small 10 nm CoFe_2O_4 spherical nanoparticles. The SAED patterns were recorded and Debye-Scherrer rings were obtained. These are shown in Figure 5d and represented as (111), (220), (311), (400), (422), (511), (440) and (531) lattice planes, which are supported by the XRD analysis. HR-TEM images of $\text{CoFe}_2\text{O}_4/\text{rGO}$ composites are shown in figure S2 (see ESI†).

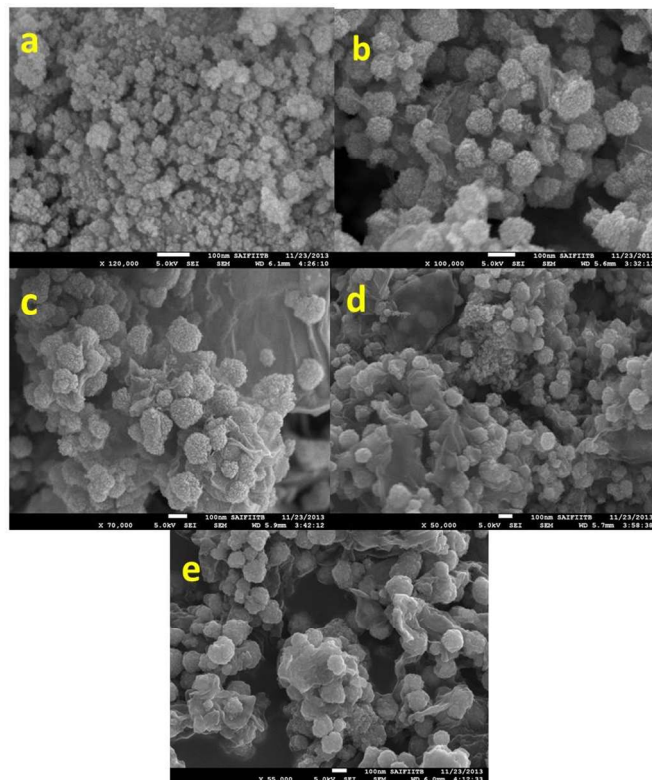


Figure 4: FESEM images for the a) pure CoFe_2O_4 , b) $\text{CoFe}_2\text{O}_4+10\%$ rGO, c) $\text{CoFe}_2\text{O}_4+20\%$ rGO, d) $\text{CoFe}_2\text{O}_4+ 30\%$ rGO, e) $\text{CoFe}_2\text{O}_4+40\%$ rGO composites.

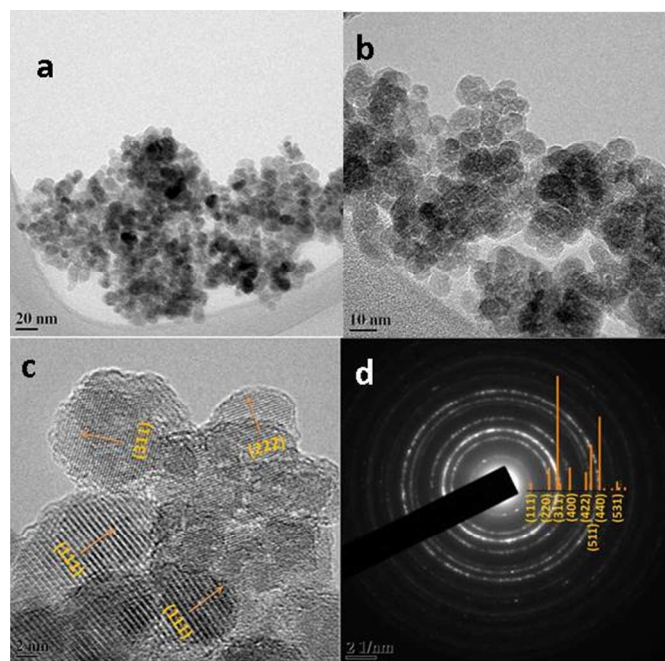


Figure 5: a & b) TEM images at different magnifications, c) High resolution images and d) SAED ring patterns for the pure porous CoFe_2O_4 nanoclusters.

Figure 6 shows the Raman spectra for the all four composites. From figure 6, the CoFe_2O_4 +10% rGO composites shows the $\text{A}_{1g} + \text{E}_g + 3\text{T}_{2g}$ bands which are confirmed the formation of CoFe_2O_4 spinel structure with space group $Fd\bar{3}m$. Furthermore, along these bands, the D and G bands at 1350 cm^{-1} and 1630 cm^{-1} are observed in all composites [30-32]. The intensity of D and G bands is very high compared to $\text{A}_{1g} + \text{E}_g + 3\text{T}_{2g}$ in all the 20, 30 and 40% graphene composites. The XRD, FTIR, FESEM-EDS, TEM and Raman spectroscopy results confirmed that the porous CoFe_2O_4 + rGO composites are pure and can successfully prepare by using the modified Hummer's method and solvothermal process.

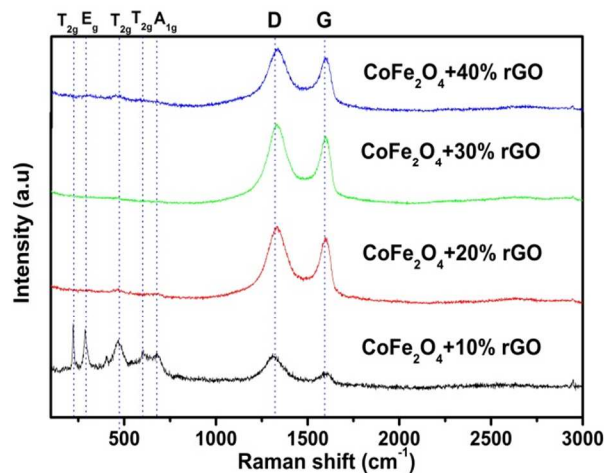


Figure 6: Raman spectra for the all CoFe_2O_4 + rGO composites.

Thermogravimetric analyses of the composite were carried out in air to know the phase changes and decomposition details. The composite was heated to 600°C at a rate of 5°C min^{-1} , the corresponding TGA curves for composites is given in Fig S3. The TGA measurement identifies the weight loss of the materials from RT to 600°C . The weight loss below 100°C is ascribed to be desorption of physically adsorbed moisture. Furthermore, weight loss between $150\text{-}200^\circ\text{C}$ is due to decomposition of polyethylene glycol and weight loss at around 300°C is ascribed to decomposition of graphene [33]. The percentage weight loss in TG curves for CoFe_2O_4 +10% rGO, CoFe_2O_4 +20% rGO, CoFe_2O_4 +30% rGO and CoFe_2O_4 +40% rGO were 12%, 24%, 31% and 38% respectively.

3.2. Electrochemical properties

Figure 7 shows the cyclic voltammetry profile for the porous CoFe_2O_4 nanoclusters and CoFe_2O_4 + rGo composite samples. From figure 7a, in the first cycle, a large cathodic peak located around 0.5 V vs. Li/Li^+ can be associated with the reduction reactions of Fe^{3+} and Co^{2+} with Li and the formation of Li_2O during the first discharge process. In the subsequent cathodic scans, CoFe_2O_4 nanoclusters show cathodic peak and anodic peak at 0.7 V and 1.5 V respectively. The intensity of peaks is changing with cycle numbers, which indicate poor stability against lithium. From figures 7b-e, all CoFe_2O_4 + rGO composites has two cathodic peaks located at 0.7 V and 1.5 V

vs. Li/Li^+ can be attributed to the reductive reaction of Fe_2O_3 and NiO to Fe and Ni metal, respectively. From figure 7f, the CoFe_2O_4 +20% rGO composite with alginate shows all redox reaction peaks for CoFe_2O_4 nanoparticles. After the first cycle, intensity of redox peaks is remaining constant which is representing that the electrode stability. In the first anodic cycle, a main broad peak at 1.6 V vs. Li/Li^+ is related to the oxidation of metallic iron and nickel to Fe^{3+} and Co^{2+} [34, 35]. Hence, CoFe_2O_4 +20% rGO composite with alginate are showing excellent electrode stability than the CoFe_2O_4 + rGO composites and pure porous CoFe_2O_4 nanoclusters with PVDF. Figure 8a shows the discharge capacity versus cycle number of pure CoFe_2O_4 nanoclusters and CoFe_2O_4 + rGO composites. From figure 8b, the discharge capacity of pure CoFe_2O_4 nanoclusters at 0.1C (91.4 mA g^{-1}) rate during the first cycle was observed as 1440 mAh g^{-1} , while at the 35th cycle it was 284 mAh g^{-1} . Approximately, 81% loss has observed in the discharge capacity of $\text{Li/CoFe}_2\text{O}_4$ nanoclusters cell. In Figure 8b, the first discharge curve shows the plateau region, which indicates the reduction reactions of metal ions and formation of Li_2O .

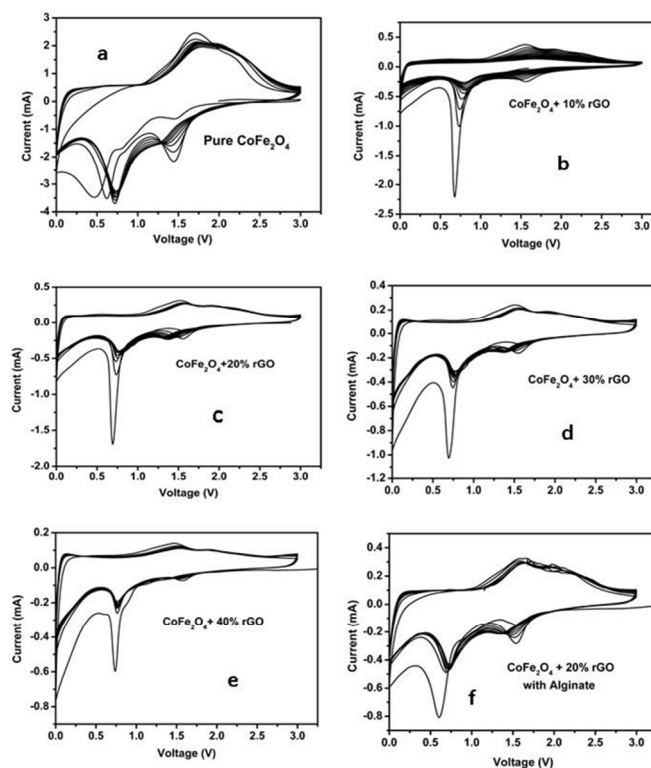


Figure 7: a-e) Cyclic voltammetry plots for the pure CoFe_2O_4 , composites with 10, 20, 30 and 40% rGO respectively and f) CoFe_2O_4 +20% rGO composite with alginate binder.

Afterwards, discharge curves do not showing any plateau region and have rapid capacity fading due to inadequate interfacial stability, which was observed earlier by cyclic voltammetry. From figure 8c, CoFe_2O_4 +10% rGO composites shows the discharge capacity of 161 mAh g^{-1} after 50 cycles. The capacity fading was observed in CoFe_2O_4 +10% rGO composites as well. From figures 8d-f, CoFe_2O_4 composite with

20, 30 and 40% graphene were showing stable discharge capacity of 940, 880 and 594 mAh g⁻¹ respectively, after 50 cycles. The CoFe₂O₄ with rGO were showing good rate capability and cycling stability due to the 2D graphene structure which will provide the conductive path for electron transportation and also it will accommodate the volume expansion while charging/discharging. Among them, CoFe₂O₄+20% rGO composites have delivered stable and high storage capacity compared to all other composites. But, it is still less than theoretical capacity of pure CoFe₂O₄ materials.

Hence, we prepared electrode with Na-alginate binder and to evaluate the cycling behavior of CoFe₂O₄+20% rGO composite. Figure 9a shows the specific capacity versus cycle number plot up to 50 cycles. From figure 9a, the CoFe₂O₄ + 20% rGO composite with alginate binder delivered stable and high capacity of 1040 mAh g⁻¹ at 0.1 C (91.4 mA g⁻¹) rate with excellent coulombic efficiency. The CoFe₂O₄/rGO composites presented the extra capacity, is due to the reversible formation and decomposition of polymeric gel-like films on the active particles [36].

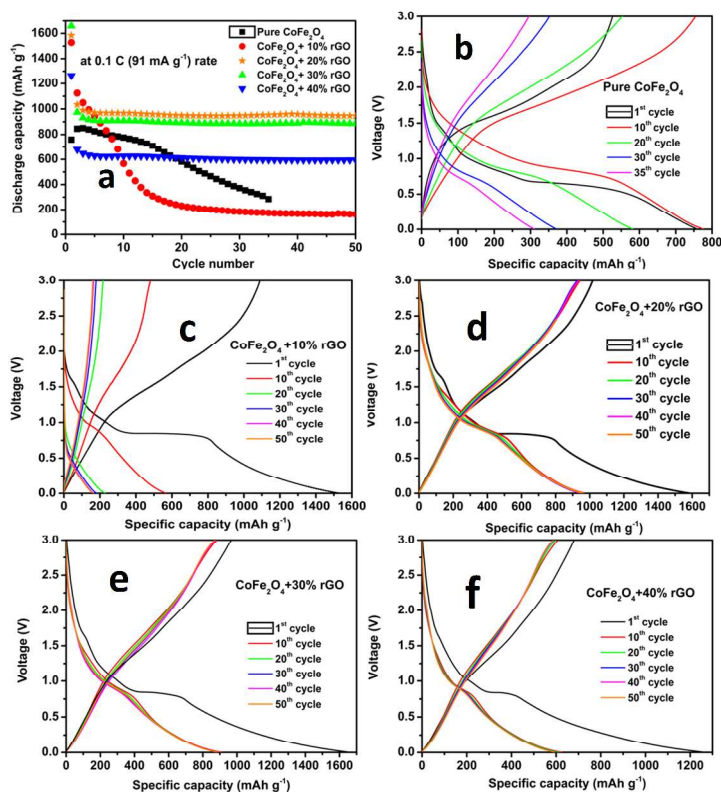


Figure 8: a) discharge capacity versus cycle number plot for pure CoFe₂O₄ and CoFe₂O₄+ rGO composites, b-f) charge- discharge curves for the pure CoFe₂O₄, composites with 10, 20, 30 and 40% rGO respectively

From figure 9b, two plateaus are observed during the first discharge, which were ascribed to the Li-intercalation and reduction of Fe³⁺ and Co²⁺, respectively. Also, from second cycle onwards, the plateau at different voltage due to reduction of metal oxides. Figure 10 shows that the rate capability plots for the CoFe₂O₄+20% rGO composites with alginate binders. Cycles were performed at different rates start from 914 mA g⁻¹ (1C), 1828 mA g⁻¹ (2C),

4570 mA g⁻¹ (5C), 9140 mA g⁻¹ (10C), 18280 mA g⁻¹ (20C) and then revert back to 1C rate. At each rate, ten cycles were run to test its retention capacity. At a very high rate of 18280 mA g⁻¹, 42.5% of original capacity was retained with high cycleability for the CoFe₂O₄+20% rGO composites with alginate binder. Discharge capacity of the anode decreases to 810, 720, 604, 460 and 380 mAh g⁻¹ when current rate increases to 1, 2, 5, 10 and 20C, respectively. The rate capability plots for the CoFe₂O₄/rGO (20%) composites with PVDF binder shown in figure S4 (see ESI†).

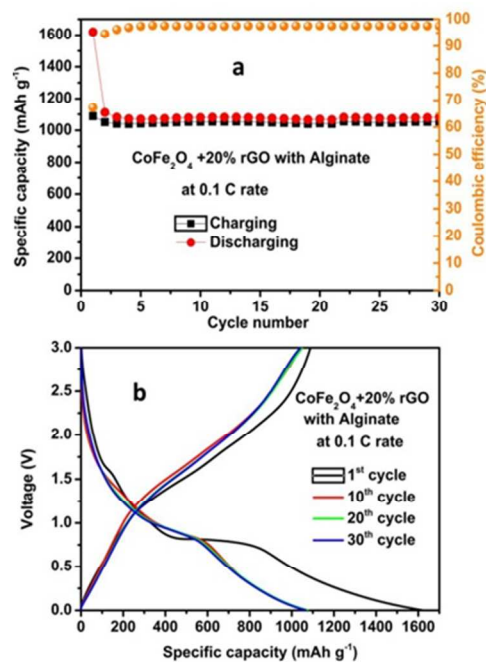


Figure 9: a) Discharge capacity versus cycle number plots and b) Galvanostatic charge-discharge curves of CoFe₂O₄+20% rGO composite with alginate binder at 0.1C rate.

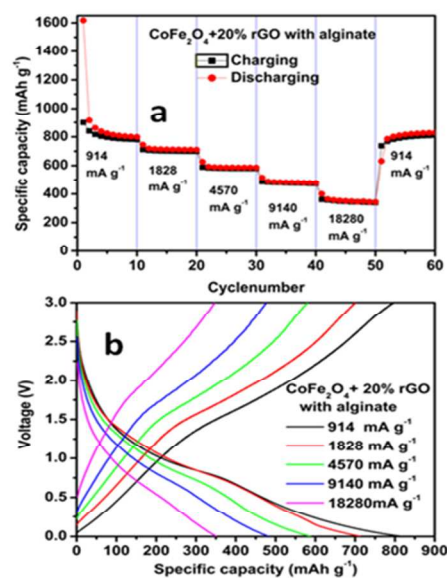


Figure 10: a) Discharge capacity versus cycle number plots and b) Galvanostatic charge-discharge curves of CoFe₂O₄+20% rGO composite with alginate binder at 0.1C rate.

In case of PVDF binder, discharge capacity of the anode decreases to 720, 680, 584, 460 and 280 mAh g⁻¹ when current rate increases to 1, 2, 5, 10 and 20C, respectively. The CoFe₂O₄ + 20% rGO composite with alginate shows superior cycle stability and capacity retention compared to the PVDF binder. The enhancement in properties might be due to the good adherence behavior between the active material surface and alginate binder. The sodium alginate has carboxyl groups on its surface, which allow bonding between outer surface of CoFe₂O₄+20% rGO composite and the binder, which are playing main role to hold the integrity of electrode during conversion reaction [25, 37]. We have confirmed the effect of alginate binder on pure CoFe₂O₄ nanoclusters by measuring charge discharge cycling (see ESI†, figure S5). From figure S4, the pure CoFe₂O₄ nanoclusters with alginate binder were showing stable capacity of 520 mAh g⁻¹ (60% of its theoretical capacity) up to 50 cycles at 0.1C rate. Similarly, pure porous CoFe₂O₄ nanoclusters with alginate binder were having high stable electrochemical performance compared with PVDF binder. It should be noted that the adding only carbon additive to active material is not a successful attempt to achieve high capacity, long cycle life and rate capability compared to using appropriate binder in conversion electrodes. In CoFe₂O₄+20% rGO composite with alginate, the alginate binder will providing the adherence properties to hold the integrity of electrode and 20% G will give the unbreakable conducting network during conversion reaction, which are the reasons behind its high electrochemical performances.

The porous capacity of CoFe₂O₄+20% rGO was determined by N₂ adsorption-desorption isotherm (Fig. S6a). The N₂ gas adsorption-desorption isotherms display the typical type IV curves and are type H3 hysteresis loop according to IUPAC (International Union of Pure and Applied Chemistry) classification. The specific surface area was calculated to be 126.04 m²/g using the Brunauer-Emmett-Teller method (BET). This behaviour shows the predominance of mesopores. This results shows more effect on desorption isotherm than adsorption isotherm because the effect of pore network shows a different behaviour of adsorption and desorption isotherms around the relative pressure P/P₀ = 0.45 (for N₂ at 77K). This leads to the forced closure of the hysteresis loop and the behaviour is referred as Tensile Strength Effect (TSE). The pore size calculation was performed on desorption branch of N₂ adsorption-desorption isotherm by Barrett-Joiner-Halenda (BJH) method. The dV/dD pore volume vs. pore diameter curve (Fig. S6b) shows broad distribution of mesopores with a sharp peak at 8 nm. Furthermore, the BJH desorption pore size distribution curves confirmed the predominance of mesopores in CoFe₂O₄/rGO [38, 39]

The dynamical properties of CoFe₂O₄+20% rGO composite electrode with PVDF and alginate binders evaluated from impedance spectroscopy measurement during the 1st cycle. Figure 10 shows the Nyquist plots for the CoFe₂O₄+20% rGO composite electrode with PVDF and alginate at different voltages. The impedance data were analyzed by using an equivalent electrical circuit model shown in Figure S7c [40-42].

It consists of electrolyte (R_e), a combined surface film and charge transfer (R_{SF+CT}) resistances with constant phase element (CPE_{SF+CT}) along with suitable diffusional component like Warburg impedance (Wd) and the intercalation capacitance (C_{im}). From Figure 11, we can observe that there is one depressed semicircle at high frequency range and can be tentatively ascribed to the migration of lithium ions through an inorganic surface film (SF) as well as charge-transfer (CT) reaction occurring at the particle-electrolyte surface. The observed depressed semicircle was fitted by using R and CPE combination.

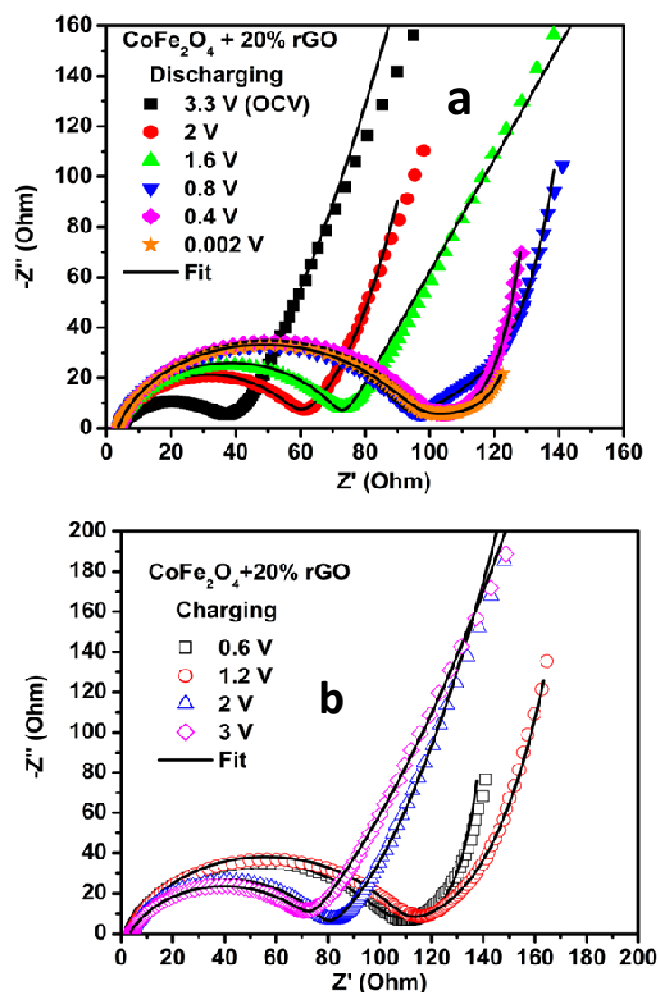


Figure 11: Nyquist plots for CoFe₂O₄+20% rGO composite electrode at a & b) discharging and charging states with PVDF

Figures 11 a & b show the Nyquist plots for the CoFe₂O₄ + 20% rGO composite electrode with PVDF at discharging and charging states respectively. In figures 10a & b, we can observe that the R_(SF+CT) increases slightly as the voltage is decreased in the discharge state and decreases in the charging state, even when the voltage is increased. The value of R_(SF+CT) increasing and decreasing during discharging and charging might be due to the solid electrolyte interface (SEI) formation/partial dissolution/re-formation [43]. Figures 12 a & b shows the

Nyquist plots for the $\text{CoFe}_2\text{O}_4+20\%$ rGO composite electrodes with alginate binder at discharging and charging states respectively. In the case of alginate binder, it is observed that the values of $R_{(\text{SF}+\text{CT})}$ at OCV (initial point of discharging state) and 3V (Final point of charging state) are almost equal. Hence, it is confirmed that the SEI of $\text{CoFe}_2\text{O}_4+20\%$ rGO composite with alginate is stable during the discharging and charging. The values of R_e and $R_{(\text{SF}+\text{CT})}$ at different voltages for pure CoFe_2O_4 , and $\text{CoFe}_2\text{O}_4+20\%$ rGO composite with PVDF and alginate binders are shown in Table S8. Furthermore, nano-sized porous structures with 2D graphene network offer good charge transfer kinetics due to their high surface to volume ratio. Therefore, the better performance of $\text{CoFe}_2\text{O}_4+20\%$ rGO with Na-alginate must be ascribed to the stability of the interfaces providing constant capacity values in long-term cycling.

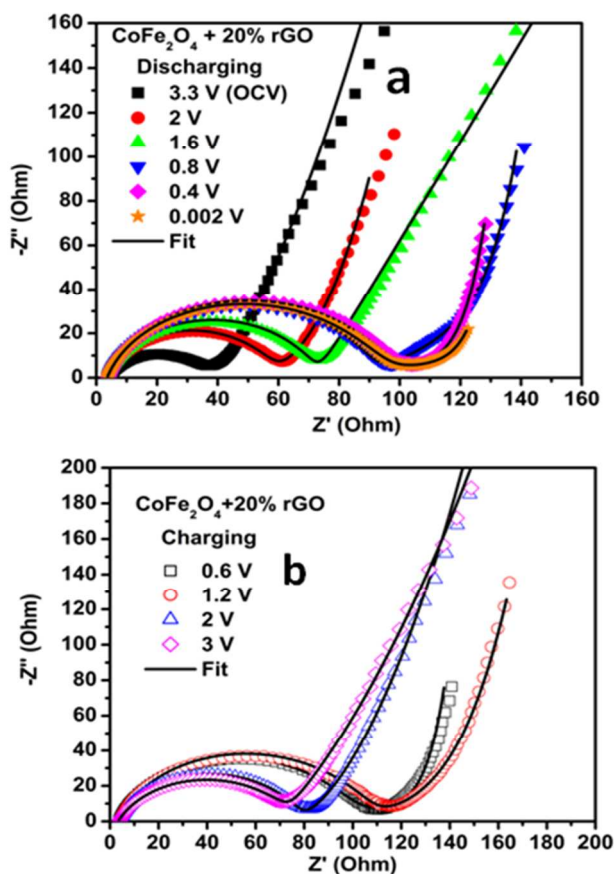


Figure 12: Nyquist plots for $\text{CoFe}_2\text{O}_4+20\%$ rGO composite electrode at a & b) discharging and charging states with alginate.

4. Conclusions

The $\text{CoFe}_2\text{O}_4/\text{rGO}$ composites were successfully synthesized using the modified Hummer's method and solvothermal processes. The phase, structure and microstructure of the prepared $\text{CoFe}_2\text{O}_4/\text{rGO}$ composites were confirmed by the XRD, FESEM-EDS, TEM and Raman spectroscopy. The $\text{CoFe}_2\text{O}_4+20\%$ rGO composites with alginate binder delivering stable maximum discharge capacity of 1040 mAh g^{-1} at 0.1C,

which is nearer to its theoretical capacity (914 mAh g^{-1}) of this material. The alginate binder hold the integrity of electrode and 20% rGO will give the electron transportation network during conversion reaction in $\text{CoFe}_2\text{O}_4+20\%$ rGO composites/alginate electrode. The stability of solid electrolyte interface (SEI) was observed by Impedance spectroscopy. Hence, we suggest that the $\text{CoFe}_2\text{O}_4+20\%$ rGO composite material with alginate is an anode material for next generation Li-ion battery applications.

Acknowledgments

Authors acknowledge SAIF, Central surface analytical facility of IIT Bombay. Dr. Pratap Kollu acknowledges DST-INSPIRE Faculty award (2012-2017).

Prof. D. K. Kim acknowledges the financial support by Basic Science Research Program through the National Research Foundation of Korea (NRF) funded by the Ministry of Education (2009-0094038).

Notes and references

^a Department of Materials Science and Engineering, Korea Advanced Institute of Science and Technology (KAIST), Daejeon 305-701, Republic of Korea. Fax: +82-42-350-3310; Tel: +82-42-350-4118; E-mail: dkkim@kaist.ac.kr

^b DST-INSPIRE Faculty, Department of Metallurgical Engineering and Materials Science, Indian Institute of Technology Bombay, Mumbai 400076, India, Tel: +91-22-2576-7603 E-mail: pratapk@iitb.ac.in

^c Centre for Nanotechnology Research, VIT University, Vellore- 632014, India; E-mail: anirmalagrace@vit.ac.in; anirmalaglady@gmail.com

^d Department of Metallurgical Engineering and Materials Science, Indian Institute of Technology Bombay, Mumbai 400076, India

† Electronic Supplementary Information (ESI) available: Experimental details and characterization: Figure S1–S8. See DOI: 10.1039/b000000x/

References

- Nazri, A.; Pistoia, G. *Lithium Batteries: Science and Technology*, Kluwer; Boston, 2004.
- W. M. Zhang, X. L. Wu, J. S. Hu, Y.G. Guo and L.J. Wang, *Adv. Funct. Mater.*, 2008, **18**, 3941-3946.
- Z. Li, X. Z. Zhan, D. Gao, D. Gao, Q. Xiao and G. Lei, *Electrochim. Acta*, 2010, **55**, 4594-4598.
- X. Zhu, Y. Zhu, S. Murali and M. D. Ruoff, *ACS Nano*, 2011, **5**, 3333-3338.
- B. Li, H. Cao, J. Shao, G. Li, M. Qu and G. Yin, *Inorg. Chem.*, 2011, **50**, 1628-1632.
- S. Y. Liu, X. Jian, Y. X. Zheng, G. S. Cao, T. J. Zhu and X. B. Zhao, *Electrochim. Acta*, 2012, **66**, 271-278.
- P. Poizot, S. Laruelle, S. Grugeon, L. Dupont and J. M. Tarascon, *Nature*, 2000, **407**, 496-499.
- H. Li, P. Balaya and J. Maier, *J. Electrochem. Soc.*, 2004, **151**, A1878-A1885.
- M. V. Reddy, G. V. Subba Rao and B. V. R. Chowdari, *Chem. Rev.*, 2013, **113**, 5364-5457.
- M. Zhu, D. Meng, C. Wang and G. Diao, *ACS Appl. Mater. Interfaces*, 2013, **5**, 6030-6037.

11. D. Bresser, E. Paillard, R. Kloepsch, S. Krueger, M. Fiedler, R. Schmitz, D. Baither, M. Winter and S. Passerini, *Adv. Funct. Mater.*, 2013, **3**, 513–523.
12. Y. Ding, Y. Yang and H. Shao, *Electrochim. Acta*, 2011, **56**, 9433–9438.
13. T. Yoon, C. Chae, Y. K. X. Zhao, H. H. Kung and J. K. Lee, *J. Mater. Chem.*, 2011, **21**, 17325–17330.
14. P. Lavela, J. L. Tirado, M. Womes and J. C. Jumas, *J. Phys. Chem. C*, 2009, **113**, 20081–20087.
15. P. Lavela, G. F. Ortiz, J. L. Tirado, E. Zhecheva, R. Stoyanova and S. Ivanova, *J. Phys. Chem. C*, 2007, **111**, 14238–14246.
16. C. Vidal-Abarca, P. Lavela and J. L. Tirado, *Solid State Ionics*, 2010, **181**, 616–622.
17. X. W. Guo, X. Lu, X. P. Fang, Y. Mao, Z. X. Wang, L. Q. Chen, X. X. Xu, H. Yang and Y. N. Liu, *Electrochem. Commun.*, 2010, **12**, 847–850.
18. P. Fen Teh, S. S. Pramana, Y. Sharma, Y. Wen Ko and S. Madhavi, *ACS Appl. Mater. Interfaces*, 2013, **5**, 5461–5467.
19. L. Wu, Q. Xiao, Z. Li, G. Lei, P. Zhang and L. Wang, *Solid State Ionics*, 2012, **215**, 24–28.
20. H. Xia, D. Zhu, Y. Fu and X. Wang, *Electrochim. Acta*, 2012, **83**, 166–174.
21. C. T. Cherian, J. Sundaramurthy, M. V. Reddy, P. S. Kumar, K. Mani, D. Pliszka, C. H. Sow, S. Ramakrishna and B. V. R. Chowdari, *ACS Appl. Mater. Interfaces*, 2013, **5**, 9957–9963.
22. Y. Wang, J. Park, B. Sun, H. Ahn and G. Wang, *Chem. Asian J.*, 2012, **7**, 1940–1946.
23. L. Ji, Z. Tan, T. Kuykendall, E. J. An, Y. Fu, V. Battaglia and Y. Zhang, *Energy Environ. Sci.*, 2011, **4**, 3611–3616.
24. Y. Deng, Q. Zhang, S. Tang, L. Zhang, S. Deng, Z. Shi and G. Chen, *Chem. Commun.*, 2011, **47**, 6828–6830.
25. I. Kovalenko, B. Zdyrko, A. Magasinski, B. Hertzberg, Z. Milicev, R. Burtovyy, I. Luzinov and G. Yushin, *Science* 2011, **334**, 75–79.
26. L. Tang, H. Chang, Y. Liu and J. Li, *Adv. Funct. Mater.*, 2012, **22**, 3083–3088.
27. H. K. Jeong, Y. P. Lee, R. J. W. E. Lahaye, M. H. Park, K. H. An, I. J. Kim, C. W. Yang, C. Y. Park, R. S. Ruoff and Y. H. Lee, *J. Am. Chem. Soc.*, 2008, **130**, 1362–1366.
28. M. Acik, G. Lee, C. Mattevi, M. Chhowalla, K. Cho and Y. J. Chabal, *Nat. Mater.*, 2010, **9**, 840–845.
29. Y. Fu and X. Wang, *Ind. Eng. Chem. Res.*, 2011, **50**, 7210–7218.
30. Z. Wang, R. T. Downs, V. Pischedda, R. Shetty, S. K. Saxena, C. S. Zha, Y. S. Zhao, D. Schiferl and A. Waskowska, *Phys. Rev. B*, 2003, **68**, 094101–094107.
31. G. V. M. Jacintho, A. G. Brolo, P. Corio, A. Z. P. Suarez and J. C. Rubim, *J. Phys. Chem. C*, 2009, **113**, 7684–7691.
32. P. Chandramohan, M. P. Srinivasan, S. Velmurugan and S. V. Narasimhan, *J. Solid State Chem.*, 2011, **184**, 89–96.
33. P. Guo, G. Zhang, J. Yu, H. Li, X.S. Zhao, *Colloid Surface A*, 2012, **395**, 168–174.
34. Z. H. Li, T. P. Zhao, X. Y. Zhan, D. S. Gao, Q. Z. Xiao and G. T. Lei, *Electrochim. Acta*, 2010, **55**, 4594–4598.
35. H. S. Kim, Y. Piao, S. H. Kang, T. Hyeon and Y. E. Sung, *Electrochem. Commun.*, 2010, **12**, 382–385.
36. L. Su, Y. Zhong and Z. Zhou, *J. Mater. Chem. A*, 2013, **1**, 15158–15166.
37. P. Ramesh Kumar and S. Mitra, *RSC Adv.* 2013, **3**, 25058–25064.
38. K. S. W. Sing, D. H. Everett, R. A. W. Haul, L. Moscou, R. A. Pierotti, J. Rouquerol and T. Siemieniowska, *Pure Appl. Chem.*, 1985, **57**, 603–619.
39. K. C. Barick, S. Singh, M. Aslam and D. Bahadur, *Micropor. Mesopor. Mater.*, 2010, **134**, 195–202.
40. G. X. Wang, L. Yang, Y. Chen, J. Z. Wang, S. Bewlay and H. K. Liu, *Electrochim. Acta*, 2006, **51**, 4634–4638.
41. H. C. Shin, W. I. Cho and H. Jang, *J. Power Sources*, 2006, **159**, 1383–1388.
42. M. V. Reddy, T. Yu, C. H. Sow, Z. X. Shen, C. T. Lim, G. V. Subba Rao and B. V. R. Chowdari, *Adv. Funct. Mater.*, 2007, **17**, 2792–2799.
43. Y. Sharma, N. Sharma, G. V. Subba Rao and B. V. R. Chowdari, *Solid state Ionics*, 2008, **179**, 587–597.